Journal of The Electrochemical Society, **161** (8) E3059-E3065 (2014)
0013-4651/2014/161(8)/E3059/7/$31.00 © The Electrochemical Society

JES Focus Issue on Mathematical Modeling of Electrochemical Systems at Multiple Scales

Crystal Surface and State of Charge Dependencies of Electrolyte Decomposition on $LiMn_2O_4$ Cathode

Nitin Kumar,[a,b,*,z] Kevin Leung,[b] and Donald J. Siegel[a,c]

[a]*Mechanical Engineering Department, University of Michigan, Ann Arbor, Michigan 48109, USA*
[b]*Sandia National Laboratories, Albuquerque, New Mexico 87185, USA*
[c]*Applied Physics Program, University of Michigan, Ann Arbor, Michigan 48109, USA*

First principles calculations are used to study the initial decomposition reactions of ethylene carbonate (EC) on the (111) surface of $LiMn_2O_4$ (LMO), a candidate for Li ion battery (LIB) cathode. Theoretical studies of interfacial reactions are particularly timely due to recent experiments on the effect of LMO crystal morphology on battery cyclability and interfacial film stability [J.-S. Kim, K. Kim, W. Cho, W. H. Shin, R. Kanno, and J. W. Choi, *Nano Lett.*, **12**, 6358–6365 (2012)]. We find that EC degradation is a two-step reaction. The first step is the rate determining reaction where a proton is abstracted from EC and transferred to the surface. The second step involves ring opening of the proton abstracted EC which turns out to have a smaller barrier. Both of these reactions are sensitive to the Li content, i.e. state of charge, of the model electrode. EC degradation via H-abstraction becomes a feasible reaction route when the cathode becomes more highly charged. Comparison with predictions on the (100) surface of LMO is discussed, and speculation on the growth of nanometer-thick interfacial layer on LMO despite its relatively modest operating potential are made in light of the reaction driving forces predicted in this work.
 [DOI: 10.1149/2.009408jes]

Manuscript submitted February 4, 2014; revised manuscript received March 17, 2014. Published March 26, 2014. This was Paper 936 from the San Francisco, California, Meeting of the Society, October 27–November 1, 2013. *This paper is part of the JES Focus Issue on Mathematical Modeling of Electrochemical Systems at Multiple Scales.*

Rechargeable lithium-ion batteries (LIBs), after their successful use in portable electronic devices, are being intensively researched[1,2] for their use in plug-in- (PHEV), hybrid- (HEV) and battery-electric vehicles (BEV). Although many different compositions have been proposed for the active cathode material in LIB, $LiMn_2O_4$ (LMO) spinel has emerged as a particularly promising candidate[2–6] due to the high abundance, low cost, safety and the environmental friendliness of manganese (Mn). However, the viability of LMO as cathode is presently hindered by issues such as capacity fade and poor cycling stability.

In this work, we use first-principles calculations to study the initial steps of electrolyte decomposition on the predominant[7] (111) surface of LMO. Until recently, the focus of theoretical work has been on other facets[8–13] of LMO due to unavailability of reasonable (111) reconstruction at that time. However, a recent theoretical work by Karim et al.[14] showed that, by choosing proper reconstruction, it is possible to obtain the (111) surface as the most stable facet of LMO. The reconstruction involves a local cation inversion[15] where under coordinated surface Mn ions are swapped with the Li ions present, just below the surface, in the bulk layer. This leads to a LMO (111) surface that has no exposed Mn. We use this prescribed[14] LMO (111) surface to study the electrolyte decomposition.

The present work explores decomposition reactions at the (111) LMO surface involving ethlyene carbonate (EC), a common LIB electrolyte solvent. The intrinsic oxidative decomposition potential of EC is much higher than the typical operating voltage of 4.3 V[16–19] for undoped LMO cathodes. Hence, electrolyte decomposition is not expected to occur on the LMO cathode under the normal battery operating conditions. Despite this, interfacial films comprised of organic fragments have been widely reported on the surfaces of LMO cathode particles.[16,20–26] Hirayama et al.[27,28] observed SEI-like thin interfacial film formation on the LMO cathodes during cycling. The possibility of electrolyte decomposition becomes greater concern in high voltage cathodes such as substituted $LiMn_{1.5}Ni_{0.5}O_4$[29,30] (LMNO) due to their larger operating potentials. In general, a mixture of EC, DMC or DEC and $LiPF_6$ on LMO are shown to yield, either on the surface or in gaseous form, LiF,[20] aldehydes,[18] acetone,[31] organic radicals,[17] polyethers, carboxylic acids,[16,32–35] and carbon dioxide.[18,26,36] Some of these species can contribute to the interfacial film observed on LMO cathode.[20,26–28,37]

Recent studies revealed that morphology[29,38,39] and surface terminations[27,28,37,40] can significantly affect the electrochemical properties of LMO electrodes. Hirayama et al.[27,28] showed that the thickness of the interfacial film on the LMO (110) surface increases with the cycling of the cell. This suggests that the electrolyte is being continuously decomposed which can be responsible for capacity fading of the battery despite the modest LMO voltage. In contrast, the LMO (111) surface exhibits a stable interfacial film.[27,28] Following these surface dependence findings of LMO cathodes, Sun et al.[37] prepared nanosheets of LMO with predominant (111) surfaces and found that these LMO cathodes exhibit durable cycling performance and high capacity retention. Understanding the surface-facet dependence of film formation on LMO cathodes may lead to strategies to minimize degradation processes in LMO-based LIB, and may shed light on the properties of other cathode materials.

Another factor that can lead to poor capacity retention and limited cyclability in LMO-based LIBs is related to Mn^{2+} dissolution in organic electrolytes stemming from disproportionation reactions.[41–44] Dissolved Mn ions can destabilize the electrolyte/electrode interface at both the anode[42,45–47] and the cathode.[27,28,48,22] The morphology[29,38,39] and surface terminations[27,28,37,40] of the active LMO cathode particles can also affect the Mn dissolution tendency. For example, LMO particles with (111) surfaces do not exhibit significant Mn dissolution.[27,28] In contrast, there is evidence to suggest that the (110) surface is vulnerable to Mn dissolution.[27,28] One possible explanation for this behavior is that the interfacial film on LMO (111) surface acts as a barrier against Mn(II), and not electron, leakage to the electrolyte. Similarly, it was shown that high voltage LMNO particles exhibited surface crystallographic planes dependent capacity fading behavior.[29]

The present work explores the surface-facet dependence of degradation mechanisms in LMO-based LIB by examining the initial stages of EC decomposition on the most stable LMO (111) facet. Our calculations reveal that EC decomposition is a two-step reaction. The first reaction is a proton (H) abstraction (H-abstraction) process which is a rate determining step. This is in agreement with the recently proposed mechanism by Borodin et al.,[49,50] which is now becoming a common theme in electrochemical oxidation reactions of electrolytes.[49–52] The second reaction involves EC ring opening and has much lower barrier than H-abstraction. The effect of varying Li content on both of these reactions is also presented. The EC decomposition products observed

*Electrochemical Society Active Member.
zE-mail: nitinkr@umich.edu

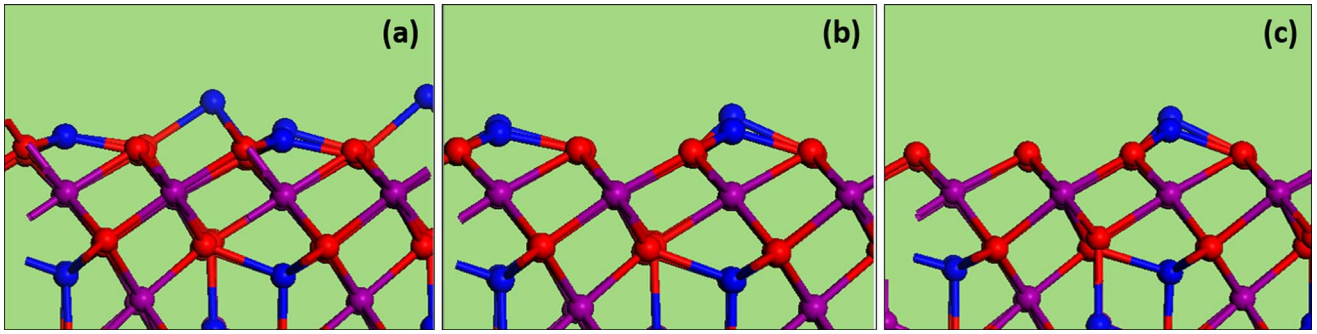

Figure 1. A side view of the LMO surface at three different lithiation states studied in the present work. (a) $LiMn_2O_4$, (b) $Li_{0.83}Mn_2O_4$ and (c) $Li_{0.67}Mn_2O_4$. Li from the surface is removed to obtain LMO surfaces with lower Li contents. Purple, dark blue and red spheres represent Mn, Li and O atoms, respectively.

in these reactions for the LMO (111) surface closely resembles to those found earlier on the (100) surface,[11,12] despite the fact that Mn ions are exposed on the pristine (100) surface but not on (111). In addition, both of these surfaces exhibit two-step EC decomposition reactions. However, the reaction route for LMO (100) is reverse of that seen for LMO (111) surface. On (100) surface, the reaction starts with EC's ring opening process and then an H-abstraction reaction occurs. These reactions are predicted to occur in the absence of PF_6^- and HF. However, the predicted decomposition products, especially the protons released, may further react to generate these fluoride species which have been shown[53] to be associated with cathode degradation.

This paper is organized as follows. Section 2 describes the computational method used in the present study. Section 3 reports the results where various reaction barriers as a function of varying Li content are presented. Further discussions on the next stages of interfacial film growth, computational method, and future direction are given in Section 4. Finally, Section 5 summarizes the paper.

Method

The static DFT+U calculations reported in this work are done using the Vienna ab initio Simulation Package (VASP).[54–56] A frozen-core projector-augmented wave (PAW) scheme[57,58] is used to treat the core electrons, with the wave functions of the valence electrons expanded in a 400 eV plane wave basis set. The PBE[59] pseudopotential is used as gradient-corrected exchange-correlation functional. The DFT+U[60] augmented treatment of Mn 3d orbitals is required to correctly model the LMO spinel. We choose U - J = 5 eV, as it was shown recently[14] to yield the correct electronic and magnetic state of the bulk LMO. All calculations are spin polarized. Both static and climbing nudge elastic band (NEB)[61] barrier calculations are performed with Γ point sampling. Some spot checking calculations are performed with higher k-points (2 × 2 × 1) and higher cutoff (550 eV). A few selected NEB barriers that are calculated using 2 × 2 × 1 k-point grids exhibits at most 0.03 eV increase in barrier height in comparison to the corresponding Γ point calculation. The effect of increasing the plane-wave cutoff energy is also minimal. The surface energy shows a small decrease of 0.01 J/m^2 when the cutoff energy is changed from 400 eV to 550 eV. Unless specifically mentioned, all atoms are allowed to relax until the forces are below a convergence threshold of 0.05 eV/Å. We use the VASPsol code[62–65] to determine the effect of solvation on reaction barriers. Finite temperature effects are predicted to be relatively small on the (100) surface[11] and hence assumed to have small effect on (111) surface as well. Our present calculation does not include the zero point energy (ZPE) correction. If included, ZPE will further lower the reaction barriers. The dimensions of the surface simulation cell are 11.69 × 12.03 × 22.55 Å^3, which allow for the two surfaces of the LMO slab to be separated by 8 Å, ensuring minimum interaction between periodic images. An additional 8 Å of vacuum is added perpendicular to the surface in cases where adsorbed molecules are present.

We use the methodology suggested by Karim et al.[14] to obtain the most stable $LiMn_2O_4$ bulk crystal and (111) surface structures. The antiferromagnetic ordering imposed is the same as in Ref. 14. The surface energy of the (111) facet is calculated (using a stoichiometric $Li_{24}Mn_{48}O_{96}$ slab) to be 0.69 J/m^2, in good agreement with that obtained (0.67 J/m^2) previously.[14] The small difference between the two results can be due to various factors. For example, in the surface energy calculations we use stricter force convergence criterion of 0.01 eV/Å, fewer k-points (2 × 2 × 1) and a thinner slab having 3 layers with no layers fixed. In contrast, Ref. 14 used 0.02 eV/Å force convergence criterion, 8 × 8 × 8 k-points sampling and a thicker 8-layer slab with middle four layer fixed.[14] The dispersion correction, not used in the surface energy calculation, is applied later to all following EC decomposition results presented. A fully self-consistent dispersion correction method (vdW-DF2) is used as implemented in VASP.[66,67]

In addition to a stoichiometric LMO model, $Li_xMn_2O_4$ slabs corresponding to different states of charge (or equivalently Li content) are examined for the cases x = 0.83 ($Li_{20}Mn_{48}O_{96}$) and x = 0.67 ($Li_{16}Mn_{48}O_{96}$) (Figure 1), by removing equal number of Li atoms from both surfaces of the LMO slab. The lattice constants for all values of "x" are kept at those of $LiMn_2O_4$. Here, x = 1.0 corresponds to an LMO based battery in a fully discharged state whereas x = 0.67 refers to a higher charged state of the battery. Figure 1 shows the simulation cells with changing Li-content, corresponding to different charge of state. We caution that, due to the finite size of the model LMO slab, most Li are removed from the surfaces and the state-of-charge estimate (i.e., "x" in $Li_xMn_2O_4$) may not correspond to those of truly bulk samples. Mn charge states are determined by monitoring the local magnetic moment.

There are some differences in computational methodology and LMO composition between this study and our previous work on LMO (100) surface.[11] In the present study, we include dispersion correction which was not used on the (100)[11] surface. A second difference is that for the DFT+U correction, we take U − J = 5 eV which is in agreement with Karim et al.'s[14] methodology. The (100) study had U − J = 4.85 eV. Nevertheless, we do not expect qualitative differences when using these new set of parameters, except that the adsorption energies of EC molecules on LMO surfaces will be larger. Another difference is that the LMO (100) surface was at a slightly higher state of charge ($Li_{0.6}Mn_2O_4$)[11] than the highest state of charge that is considered for the present LMO (111) surface i.e. $Li_{0.67}Mn_2O_4$. Lastly, the (100) surface had exposed Mn ions on the surface. However, the (111) LMO surface does not have any Mn ions on the surface.

Results

First we focus on a (111) slab with stoichiometry $Li_{0.67}Mn_2O_4$. The EC molecule physisorbs exothermally on this surface (Figure 2). It undergoes a small distortion where the bond angle between carbonyl carbon and ethylene carbon changes by 6°. The energy for this intact configuration is calculated to be −1.1 eV. The molecule is oriented

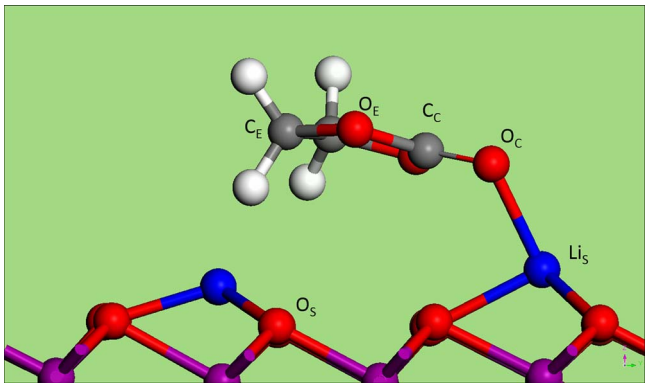

Figure 2. Physisorbed (Intact) EC molecule atop $Li_{0.67}Mn_2O_4$ (111) surface. The energy for this configuration is −1.1 eV. The surface Lithium (Li_S), surface oxygen (O_S), carbonyl oxygen (O_C), carbonyl carbon (C_C), ethylene oxygen (O_E) and ethylene carbon (C_E) are labeled. Purple, dark blue, red, gray and white spheres represent Mn, Li, O, C and H atoms, respectively.

parallel to the surface with O_C forming a strong bond (∼1.94 Å) with a surface Li (Li_S).

The oxidative decomposition of this adsorbed EC is found to be a two-step reaction. The first step is an H-abstraction process (Figure 3) where one of the H from EC that was pointing toward the surface is detached from an ethylene carbon (C_E) atom. This H ends up covalently bonding with a surface oxygen (O_S) which leads to a hydroxyl (–OH) formation on the surface. The starting configuration in this reaction is the physisorbed EC molecule, i.e. the intact configuration. The final product is a metastable H-abstracted configuration with a −0.84 eV energy. The transition state (TS) has H equidistant from C_E and O_S (1.3 Å) and the barrier for this reaction is +0.62 eV. A small barrier (+0.12 eV) follows the TS which is primarily due to the rotation of the –OH. In this H-abstraction reaction, the final metastable configuration is obtained by fixing the H atom and allowing all other atoms to relax. If H is also allowed to relax then H-abstracted EC is found to move away from the reaction site.

The next step of the reaction involves breaking the covalent bond between carbonyl carbon (C_C) and ethylene oxygen (O_E), i.e. the C_C-O_E bond (Figure 4), in the H-abstracted EC configuration (Figure 3). In the beginning, EC undergoes some rearrangement preparing itself for the C_C-O_E bond breaking event. This reorientation is followed by ring opening and further reorganization of the broken EC fragment. The reaction ends with the broken C_C covalently bonding (∼1.3 Å) with another O_S and the broken O_E bonding with a neighboring Li_S (∼2.0 Å). The final configuration, with EC decomposed, is strongly exothermic by −1.84 eV with respect to the intact configuration. The barrier for this second reaction is relatively small (+0.35 eV) and it is mainly due to rearrangement of the H-abstracted EC molecule.

We find that both H-abstraction and C_C-O_E bond breaking reactions involve charge transfer. The charge transfer can be deduced by changes in the magnetization of the Mn ions. A total of three Mn ions undergo a change in the charge state from Mn(IV) to Mn(III) indicating that 3 electrons have transferred during the complete EC decomposition reaction. The first two electron transfers are observed during the H-abstraction (Figure 3). Both of these electrons end up at Mn ions which are located in the bulk. The first electron transfer occurs right at the transition state (TS) of the reaction. Thereafter another electron transfers in the following steps of EC rearrangement. The final electron transfer occurs when the C_C-O_E is broken and C_C prepares to bond with O_S (Figure 4). In this case, the electron ends up at the Mn ion (shown by yellow arrow in Image 2 of Figure 4) which is just below the surface and is covalently bonded to the O_S ion which forms a bond with the undercoordinated C_C atom later in the reaction.

Next we consider the effect of Li-content on the two reactions (Figure 5, Table I) described above. Again we emphasize that our slab model is of finite thickness and hence the Li-content variation of the battery may not truly reflect the state of charge of bulk samples. An estimate of the reaction rate, ignoring entropic effects and assuming Arrhenius behavior of the reactions with typical molecular

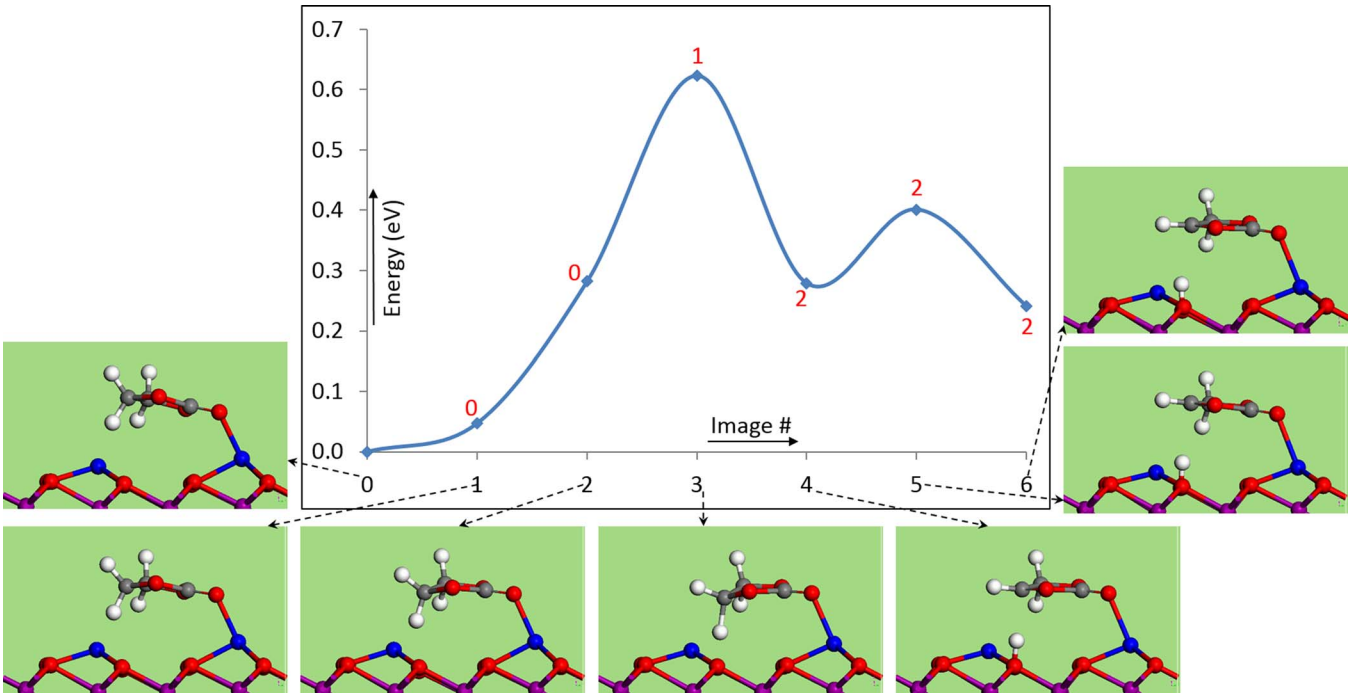

Figure 3. The energy profile for H-abstraction from EC on (111) surface of $Li_{0.67}Mn_2O_4$ cathode, computed at T = 0 K using the NEB method. NEB captures explicitly the H-abstraction with energy barrier being +0.62 eV. The second small barrier of +0.12 eV (image 4 to image 6) corresponds to rotation of the surface hydroxyl (-OH) group. The final product, i.e. metastable H-abstracted configuration, is obtained by fixing the H that is transferred from EC to surface oxygen. Numbers shown in red correspond to number of electrons transferred, with respect to the intact configuration, from EC to the LMO slab.

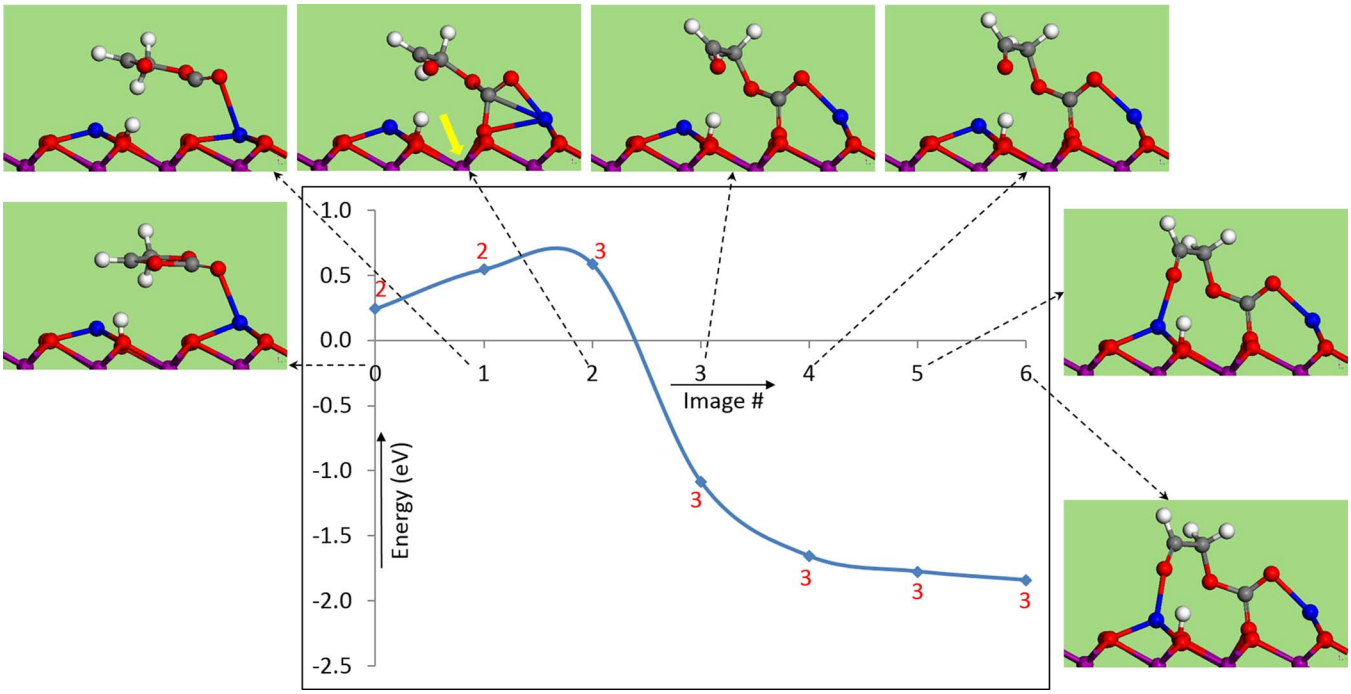

Figure 4. The energy profile for O-CO breaking starting from H-abstracted EC on (111) surface of $Li_{0.67}Mn_2O_4$ cathode, computed at T = 0 K using the NEB method. The barrier for this reaction is +0.35 eV. The zero on the y-axis corresponds to the energy of the intact configuration. Numbers shown in red correspond to number of electrons transferred, with respect to the intact configuration, from EC to the LMO slab. The yellow arrow, in Image 2, indicates the location of Mn ion that gained an e- which was transferred from EC.?vsp -5pt?

vibrational prefactor of 10^{12} /sec at room temperature, is also reported in Table I. The barrier for H-abstraction decreases with decreasing Li content. A fully discharged battery, i.e. $LiMn_2O_4$, has the highest barrier of +1.18 eV (Figure 5) which corresponds to a reaction rate of 10^{-8} (reactions/sec). However, as charging proceeds and reaches a higher charged state ($Li_{0.67}Mn_2O_4$), the H-abstraction barrier decreases to +0.62 eV (Figure 3). This reduction in barrier exponentially affects the reaction rate where it increases 10^9 times to 10^1 (reactions/sec). This reaction is well within the typical charging/discharging rate of 1 C, i.e. about an hour. The metastable H-abstracted configurations for other stoichiometries (i.e. $LiMn_2O_4$ and $Li_{0.83}Mn_2O_4$) are obtained by allowing all atoms to relax. The

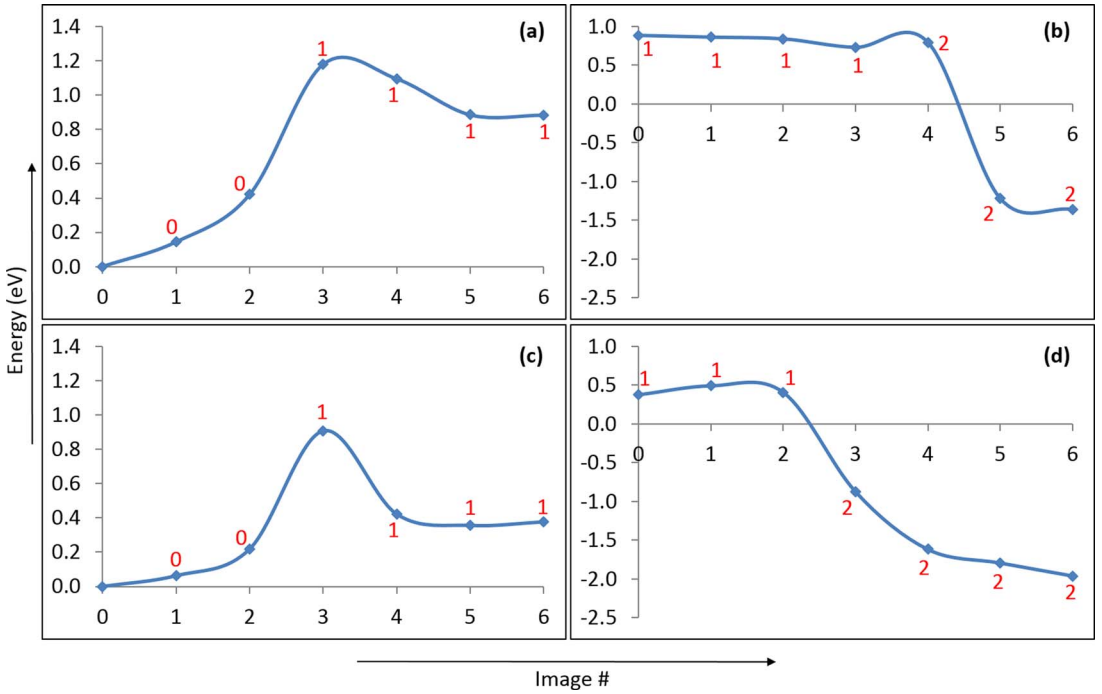

Figure 5. The energy profile for H-abstraction (a and c) and O-CO breaking (b and d) for $LiMn_2O_4$ (a and b) and $Li_{0.83}Mn_2O_4$ (c and d) cathode surfaces, computed at T = 0 K using the NEB method. The metastable H-abstracted configurations are obtained by allowing all atoms to relax. Numbers shown in red correspond to number of electrons transferred, with respect to the intact configuration, to the LMO slab during the reactions.

Table I. H-abstraction and C_C-O_E bond breaking energy barriers as the Li content of the LMO cathode varies. An estimate of the reaction rate, ignoring entropic effects and assuming Arrhenius behavior of the reaction with typical molecular vibrational prefactor of 10^{12} /sec at room temperature, is also reported. The number of electrons (# e^-) transferred from EC to the LMO slab is given for all reactions and surfaces. *: The barrier is calculated with respect to the intact configuration. †: The barrier is calculated with respect to the H-abstracted EC configuration.

	H-Abstraction			C_C-O_E Breaking		
System↓	$\Delta E_{barrier}$ (eV)*	Reaction Rate at T = 300 K (sec^{-1})	# e^-	$\Delta E_{barrier}$ (eV)†	Reaction Rate at T = 300 K (sec^{-1})	# e^-
$Li_{1.0}Mn_2O_4$	+1.18	$\sim 10^{-8}$	1	+0.00	$\sim 10^{12}$	1
$Li_{0.83}Mn_2O_4$	+0.91	$\sim 10^{-4}$	1	+0.12	$\sim 10^{9}$	1
$Li_{0.67}Mn_2O_4$	+0.62	$\sim 10^{1}$	2	+0.35	$\sim 10^{6}$	1

H-abstracted EC does not leave the reaction site, as observed for the $Li_{0.67}Mn_2O_4$ surface, on these other stoichiometries.

A similar Li-content dependence on the barrier, although smaller, is seen for the second reaction, i.e. C_C-O_E breaking. The fully discharge cathode, i.e. $LiMn_2O_4$, has nearly a barrierless ring opening of the H-abstracted EC. A small increase in this barrier, from barrierless to +0.35 eV, is observed when the cell reaches a higher charged state, i.e. $Li_{0.67}Mn_2O_4$. This is a much faster reaction than H-abstraction process with 10^6 reactions/sec. Hence, the H-abstraction barrier decreases whereas the EC's ring opening barrier increases with decreasing Li content as the battery charges from fully discharged state. Such Li-content dependence is reasonable because the reaction involves EC oxidation, which is facilitated by higher states of charge.

The number of electrons transferred from EC also varies with the changing Li-content of the cathode (Table I). A fully discharged LMO cell has one electron transferred during H-abstraction. However, when the cell reaches the higher charge state ($Li_{0.67}Mn_2O_4$) there are two electrons transferred from EC. In contrast, the second reaction of C_C-O_E breaking is associated with only one electron transfer for all the Li-content states studied here. Note that EC degradation on LMO (111) surface starts with proton and electron transfer from EC, in agreement with the predicted reaction pathway in electrochemical oxidation of solvent molecules in the absence of an electrode.[49–52]

The effect of solvation on reaction barrier is determined using the VASPsol code[62–65] without further relaxing the geometry. The bulk dielectric constant of EC and DMC mixture ($\epsilon = 40$) is used to represent a commonly used electrolyte for LIB. However, the dielectric constant decreases as the interface is approached. To explore the impact of this reduction in dielectric constant, the effect of solvation on reaction barrier is also calculated for $\epsilon = 4.2$ (ether).[50] We find that the rate limiting H-abstraction reaction exhibits a small decrease in barrier ~0.1 eV (for $\epsilon = 40$) and ~0.02 eV (for $\epsilon = 4.2$) when solvation is employed. This agrees well with our previous predictions[11] for (100) LMO surface.

We have also studied a small number of other candidate EC decomposition products (Figure 6). One of these is formed via C_C-O_E bond breaking without initial H-abstraction. This results in an endothermic configuration (Figure 6a) with energy of +0.74 eV with respect to the intact configuration. In comparison, the H-abstracted C_C-O_E bond broken EC configuration was found to be highly exothermic (−1.84 eV). Geometrically the two configurations, without and with H-abstraction, are similar. But the energetics clearly indicates that the occurrence of H-abstraction as a first reaction step might be crucial in EC degradation. Another decomposition candidate corresponds to breaking the C_E-O_E bond after H-abstraction (Figure 6b). This configuration results in an endothermic product with energy of +0.56 eV compared to the intact configuration, and is likewise much less favorable than the H-abstracted C_C-O_E pathway. The unfavorable thermodynamics of this alternative pathway suggests that, after the critical H-abstraction reaction, C_C-O_E bond breaking is a more plausible reaction route than C_E-O_E bond breaking.

The products obtained after EC decomposition on LMO (111) surface are similar to that observed in earlier work[11,12] on LMO (100) surface. On both surfaces, EC loses a proton and a C_C-O_E bond is broken. However, the order of the reaction sequence is reversed on these two surfaces. As shown above, the (111) surface has a rate determining H-abstraction followed by EC ring opening that constitute C_C-O_E bond breaking. On the (100) surface, the first step of the reaction is C_C-O_E bond breaking followed by an H-abstraction. The initial C_C-O_E bond breaking event is found to yield a low (+0.48 eV) barrier on the (100) surface. However, the barriers for H-abstraction on both surfaces are similar (~+0.6 eV).

Discussion

The decomposition reactions described above result in fragmentation of EC which can cover the complete LMO cathode surface, thus forming the precursor to the experimentally observed interfacial film.[27,28] We have shown that EC directly adsorbed on the (100) and (111) surfaces of LMO are readily oxidized (Ref. 11 and this work). The reactions are highly exothermic, releasing almost 2 eV, regardless of whether Mn ions are exposed on the surface. The large

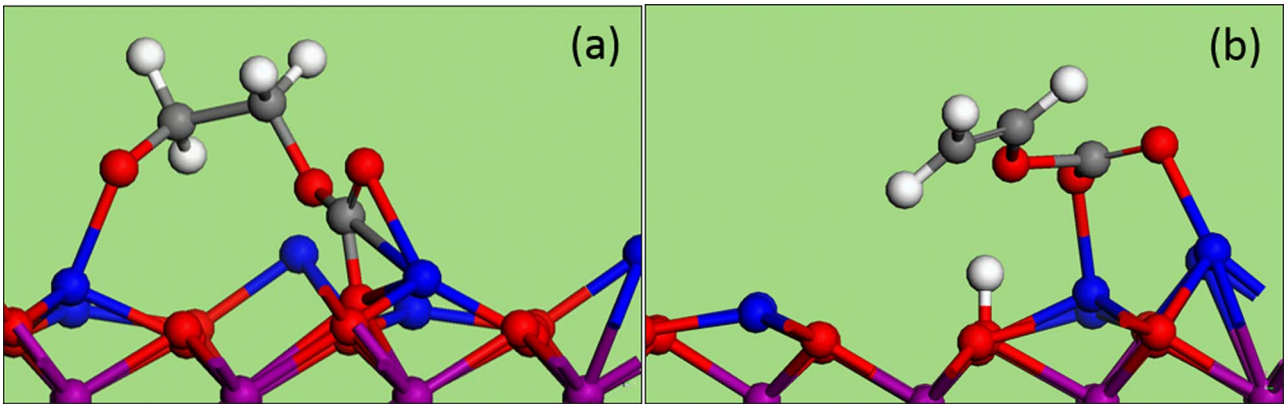

Figure 6. Other decomposition products considered. (a) C_C-O_E bond breaking without H-abstraction results in a broken EC fragment with an energy of +0.74 eV with respect to the intact configuration. (b) H-abstracted C_E-O_E bond broken configuration has energy of +0.56 eV with respect to the intact configuration.

thermodynamic driving forces apparently stem from the simultaneous donation of protons to the surface and formation of C-O bonds with the surface; either step alone does not lead to significant exothermicity and may in fact be endothermic. In stark contrast, EC in bulk electrolyte environment, outside the interfacial layer, is not oxidized at lower than 4.55 V (Table 4, Ref. 50) even when counter-ion effects and cooperative EC reaction pathways are taken into account. In other words, EC oxidation in the bulk electrolyte is not favorable under LMO operating conditions. It is tempting to speculate on the intermediate regime based on our computational insights. We hypothesize that further EC oxidation on a layer of decomposed electrolyte fragments proceed in a way similar to that on the bare LMO surface; the electrolyte fragments covering the electrode should be more reactive toward the electrolyte than intact EC (or DMC/DEC cosolvent) molecules in the bulk liquid. It is also possible that the protonated surface will release water and dissolved Mn ions, further yielding reactive species close to the electrode surface. Moreover, our present predictions do not allow us to distinguish the next stage of EC oxidation on different LMO facets. It will be interesting to study the reactions of the electrolyte on surfaces already covered with electrolyte decomposition fragments, which is crucial for comparison with experiments.

In H-abstraction, the simultaneous occurrence of electron and proton transfer at the TS correspond to a well-known class of reactions called proton coupled electron transport (PCET) reactions.[68–70] The proton transfer reaction rates for these PCET reactions are proportional to the electron coupling matrix element. Since we are using the PBE functional, this matrix element can be overestimated and hence the H-abstraction barrier obtained in the present work can be overestimated as well.

An important component of the real battery environment is salt. The counter ions of salts can affect the EC degradation reactions as indicated by experimentally observed LiF[20] on LMO surface. Both electrolyte interaction with the interfacial film and the role of salt on EC decomposition will be pursued in future. Modeling explicit solvent and salt in contact with the electrode surfaces will also allow inclusion of net surface charges on the electrode surfaces.[71] The ability to incorporate the net charge on the electrode surface will allow exploration of the effect of the zeta potential, an experimentally hard to determine quantity, on the reaction energetics presented in this work.

Electrolyte degradation is a much bigger problem for high voltage cathodes, e.g. substituted $LiMn_{1.5}Ni_{0.5}O_4$ (LMNO). Interestingly, as seen for the LMO cathode, LMNO also exhibit surface morphology and termination dependent[29] electrochemical behavior. A deeper understanding of EC degradation on LMO will pave a path for analyzing electrolyte decomposition reactions on LMNO cathodes.

Summary

We have studied the initial decomposition route of ethylene carbonate (EC) on spinel $Li_xMn_2O_4$ (or LMO) (111) surface for varying Li content, i.e. state of charge. These reactions could be precursor to the interfacial film formation seen on this cathode.[16,20–26] The study begins with discussing EC decomposition atop $Li_{0.67}Mn_2O_4$ cathode. The first step in EC decomposition constitutes a proton abstraction where an H atom is transferred from EC to surface oxygen ions forming a –OH group. Along with this, two electrons are also transferred from EC to the LMO electrode. The first electron transfer occurs at the transition state of the reaction and subsequently second electron transfers when H-abstracted EC relaxes. The barrier for this reaction is +0.62 eV, which corresponds to 10^1 reactions/sec. The reaction that follows the H-abstraction is comprised of EC reorientation and subsequently covalent bond breaking between carbonyl carbon (C_C) and ethylene oxygen (O_E) resulting in ring opening of the EC molecule. This reaction has a relatively smaller barrier of +0.35 eV, corresponding to 10^6 reactions/sec. One more electron transfer occurs during this part of the reaction. Hence, we find a total of three electrons transferred from EC to the surface in the decomposition of EC on the $Li_{0.67}Mn_2O_4$ (111) facet. When these reactions are compared to a typical charging/discharging rate of the battery i.e. 1C, which translates to about an hour, H-abstraction appears to be a crucial mode of EC decomposition on LMO (111) cathode surface.

We have also studied the effect of changing Li content (or state of charge) of the battery on the two reaction barriers. As Li is successively removed from the surface of a fully discharged $LiMn_2O_4$ slab, the rate determining H-abstraction barrier of the EC oxidation reaction decreases significantly, from +1.18 eV to 0.62 eV when 33% of Li have been removed from the surface. In terms of reaction rate, the change in rate determining H-abstraction reaction barrier translates to an increase of 10^9 times to 10^1 reactions/sec, which is well within the typical battery charging/discharging rate of 1 C, i.e. about an hour. Two to three electrons are transferred in H-abstraction and one electron in EC ring opening reaction. The barrier associated with the subsequent, EC ring opening reaction varies with Li content in the opposite direction, increasing from zero to +0.35 eV. However, this process is not rate-limiting.

The first decomposition events that are presented in this work are kinetically favorable, at least for some Li-coverages. The products obtained in these reactions are similar to those seen on (100) surface. However, experimentally[27,28,39] the two surfaces behave differently when LIB is cycled. Hence, further investigations are required to find subsequent reactions that may help in distinguishing electrolyte interaction with and Mn(II) ion dissolution from the (100) and (111) LMO surfaces.

Acknowledgment

We thank Dr. Kristin A. Persson for sharing Ref. 14 prior to its publication, and Dr. Richard Hennig for sharing the VASPsol code.[62–65]

This work was supported by the U.S. Department of Energy's U.S.-China Clean Energy Research Center for Clean Vehicles, grant no. DE-PI0000012. Sandia National Laboratories is a multiprogram laboratory managed and operated by Sandia Corporation, a wholly owned subsidiary of Lockheed Martin Corporation, for the U.S. Department of Energy's National Nuclear Security Administration under contract DE-AC04-94AL85000. This research used resources of the National Energy Research Scientific Computing Center, which is supported by the Office of Science of the U.S. Department of Energy under Contract No. DE-AC02-05CH11231.

References

1. J. B. Goodenough, *Acc. Chem. Res.*, **46**, 1053 (2013).
2. A. Manthiram, *J. Phys. Chem. Lett.*, **2**, 176 (2011).
3. M. M. Thackeray, W. I. F. David, P. G. Bruce, and J. B. Goodenough, *Mater. Res. Bull.*, **18**, 461 (1983).
4. M. M. Thackeray, *Prog. Solid State Chem.*, **25**, 1 (1997).
5. G. Ceder, A. Van der Ven, and M. K. Aydinol, *JOM*, **50**, 35 (1998).
6. P. G. Bruce, B. Scrosati, and J.-M. Tarascon, *Angew. Chem. Int. Ed.*, **47**, 2930 (2008).
7. M.-R. Huang, C.-W. Lin, and H.-Y. Lu, *Appl. Surf. Sci.*, **177**, 103 (2001).
8. R. Benedek and M. M. Thackeray, *Phys. Rev. B*, **83**, 195439 (2011).
9. R. R. Maphanga, S. C. Parker, and P. E. Ngoepe, *Surf. Sci.*, **603**, 3184 (2009).
10. C. Y. Ouyang, Ž. Šljivančanin, and A. Baldereschi, *Phys. Rev. B*, **79**, 235410 (2009).
11. K. Leung, *J. Phys. Chem. C*, **116**, 9852 (2012).
12. K. Leung, *J. Phys. Chem. C*, **117**, 1539 (2012).
13. R. Benedek, M. M. Thackeray, J. Low, and T. Bučko, *J. Phys. Chem. C*, **116**, 4050 (2012).
14. A. Karim, S. Fosse, and K. A. Persson, *Phys. Rev. B*, **87**, 075322 (2013).
15. S. C. Parker, P. M. Oliver, N. H. De Leeuw, J. O. Titiloye, and G. W. Watson, *Phase Transit.*, **61**, 83 (1997).
16. T. Eriksson, A. M. Andersson, A. G. Bishop, C. Gejke, T. Gustafsson, and J. O. Thomas, *J. Electrochem. Soc.*, **149**, A69 (2002).
17. S. Matsuta, Y. Kato, T. Ota, H. Kurokawa, S. Yoshimura, and S. Fujitani, *J. Electrochem. Soc.*, **148**, A7 (2001).
18. M. Moshkovich, M. Cojocaru, H. E. Gottlieb, and D. Aurbach, *J. Electroanal. Chem.*, **497**, 84 (2001).
19. K. Xu, *Chem. Rev.*, **104**, 4303 (2004).
20. D. Aurbach, K. Gamolsky, B. Markovsky, G. Salitra, Y. Gofer, U. Heider, R. Oesten, and M. Schmidt, *J. Electrochem. Soc.*, **147**, 1322 (2000).
21. Y. Matsuo, R. Kostecki, and F. McLarnon, *J. Electrochem. Soc.*, **148**, A687 (2001).
22. K. Edström, T. Gustafsson, and J. O. Thomas, *Electrochimica Acta*, **50**, 397 (2004).
23. J. Lei, L. Li, R. Kostecki, R. Muller, and F. McLarnon, *J. Electrochem. Soc.*, **152**, A774 (2005).
24. A. Würsig, H. Buqa, M. Holzapfel, F. Krumeich, and P. Novák, *Electrochem. Solid-State Lett.*, **8**, A34 (2005).

25. F. Simmen, A. Hintennach, M. Horisberger, T. Lippert, P. Novák, C. W. Schneider, and A. Wokaun, *J. Electrochem. Soc.*, **157**, A1026 (2010).
26. F. Simmen, A. Foelske-Schmitz, P. Verma, M. Horisberger, T. Lippert, P. Novák, C. W. Schneider, and A. Wokaun, *Electrochimica Acta*, **56**, 8539 (2011).
27. M. Hirayama, N. Sonoyama, M. Ito, M. Minoura, D. Mori, A. Yamada, K. Tamura, J. Mizuki, and R. Kanno, *J. Electrochem. Soc.*, **154**, A1065 (2007).
28. M. Hirayama, H. Ido, K. Kim, W. Cho, K. Tamura, J. Mizuki, and R. Kanno, *J. Am. Chem. Soc.*, **132**, 15268 (2010).
29. K. R. Chemelewski, E.-S. Lee, W. Li, and A. Manthiram, *Chem. Mater.*, **25**, 2890 (2013).
30. R. Santhanam and B. Rambabu, *J. Power Sources*, **195**, 5442 (2010).
31. J. Ufheil, A. Würsig, O. D. Schneider, and P. Novák, *Electrochem. Commun.*, **7**, 1380 (2005).
32. K. Kanamura, S. Toriyama, S. Shiraishi, M. Ohashi, and Z. Takehara, *J. Electroanal. Chem.*, **419**, 77 (1996).
33. K. Kanamura, T. Umegaki, M. Ohashi, S. Toriyama, S. Shiraishi, and Z. Takehara, *Electrochimica Acta*, **47**, 433 (2001).
34. T. Matsushita, K. Dokko, and K. Kanamura, *J. Power Sources*, **146**, 360 (2005).
35. L. Yang, B. Ravdel, and B. L. Lucht, *Electrochem. Solid-State Lett.*, **13**, A95 (2010).
36. F. Joho and P. Novák, *Electrochimica Acta*, **45**, 3589 (2000).
37. W. Sun, F. Cao, Y. Liu, X. Zhao, X. Liu, and J. Yuan, *J. Mater. Chem.*, **22**, 20952 (2012).
38. K. R. Chemelewski, D. W. Shin, W. Li, and A. Manthiram, *J. Mater. Chem. A*, **1**, 3347 (2013).
39. J.-S. Kim, K. Kim, W. Cho, W. H. Shin, R. Kanno, and J. W. Choi, *Nano Lett.*, **12**, 6358 (2012).
40. J. Velmurugan, R. Garcia, and N. Missert, *Submitt. Nano Lett.*
41. J. C. Hunter, *J. Solid State Chem.*, **39**, 142 (1981).
42. A. Blyr, C. Sigala, G. Amatucci, D. Guyomard, Y. Chabre, and J.-M. Tarascon, *J. Electrochem. Soc.*, **145**, 194 (1998).
43. R. J. Gummow, A. de Kock, and M. M. Thackeray, *Solid State Ion.*, **69**, 59 (1994).
44. K. Ozawa, *Lithium Ion Rechargeable Batteries: Materials, Technology, and New Applications*, Wiley-VCH Verlag GmbH & Co. KGaA (2010).
45. A. Manthiram, A. V. Murugan, A. Sarkar, and T. Muraliganth, *Energy Environ. Sci.*, **1**, 621 (2008).
46. C. Zhan, J. Lu, A. Jeremy Kropf, T. Wu, A. N. Jansen, Y.-K. Sun, X. Qiu, and K. Amine, *Nat. Commun.*, **4**, 2437 (2013).
47. K. Leung and J. L. Budzien, *Phys. Chem. Chem. Phys.*, **12**, 6583 (2010).
48. P. Arora, R. E. White, and M. Doyle, *J. Electrochem. Soc.*, **145**, 3647 (1998).
49. O. Borodin and T. R. Jow, *ECS Trans.*, **33**, 77 (2011).
50. O. Borodin, W. Behl, and T. R. Jow, *J. Phys. Chem. C*, **117**, 8661 (2013).
51. L. Xing, O. Borodin, G. D. Smith, and W. Li, *J. Phys. Chem. A*, **115**, 13896 (2011).
52. Y. Wang, L. Xing, W. Li, and D. Bedrov, *J. Phys. Chem. Lett.*, **4**, 3992 (2013).
53. D. Aurbach, B. Markovsky, G. Salitra, E. Markevich, Y. Talyossef, M. Koltypin, L. Nazar, B. Ellis, and D. Kovacheva, *J. Power Sources*, **165**, 491 (2007).
54. G. Kresse and J. Furthmüller, *Phys. Rev. B*, **54**, 11169 (1996).
55. G. Kresse and J. Furthmüller, *Comput Mater Sci*, **6**, 15 (1996).
56. J. Paier, M. Marsman, and G. Kresse, *J. Chem. Phys.*, **127**, 024103 (2007).
57. G. Kresse and D. Joubert, *Phys. Rev. B*, **59**, 1758 (1999).
58. P. E. Blöchl, *Phys Rev B*, **50**, 17953 (1994).
59. J. P. Perdew, K. Burke, and M. Ernzerhof, *Phys. Rev. Lett.*, **78**, 1396 (1997).
60. S. L. Dudarev, G. A. Botton, S. Y. Savrasov, C. J. Humphreys, and A. P. Sutton, *Phys. Rev. B*, **57**, 1505 (1998).
61. G. Henkelman, B. P. Uberuaga, and H. Jónsson, *J. Chem. Phys.*, **113**, 9901 (2000).
62. K. Mathew, R. Sundararaman, K. Letchworth-Weaver, T. A. Arias, and R. G. Hennig, *J. Chem. Phys.*, **140**, 084106 (2014).
63. S. A. Petrosyan, A. A. Rigos, and T. A. Arias, *J. Phys. Chem. B*, **109**, 15436 (2005).
64. K. Letchworth-Weaver and T. A. Arias, *Phys. Rev. B*, **86**, 075140 (2012).
65. D. Gunceler, K. Letchworth-Weaver, R. Sundararaman, K. A. Schwarz, and T. A. Arias, *Model. Simul. Mater. Sci. Eng.*, **21**, 074005 (2013).
66. M. Dion, H. Rydberg, E. Schröder, D. C. Langreth, and B. I. Lundqvist, *Phys. Rev. Lett.*, **92**, 246401 (2004).
67. J. Klimeš, D. R. Bowler, and A. Michaelides, *Phys. Rev. B*, **83**, 195131 (2011).
68. J. M. Mayer, *Annu. Rev. Phys. Chem.*, **55**, 363 (2004).
69. S. Hammes-Schiffer and A. V. Soudackov, *J. Phys. Chem. B*, **112**, 14108 (2008).
70. I. Navrotskaya, A. V. Soudackov, and S. Hammes-Schiffer, *J. Chem. Phys.*, **128**, 244712 (2008).
71. K. Leung and C. M. Tenney, *J. Phys. Chem. C*, **117**, 24224 (2013).